SHADE: A Multilevel Bayesian Framework for Modeling Directional Spatial Interactions in Tissue Microenvironments

Joel Eliason*[1], Michele Peruzzi[2], and Arvind Rao[1,2,3,4]

[1]Department of Computational Medicine and Bioinformatics, University of Michigan, USA

[2]Department of Biostatistics, University of Michigan, USA

[3]Department of Biomedical Engineering, University of Michigan, USA

[4]Department of Radiation Oncology, University of Michigan, USA

November 23, 2025

Abstract

Motivation: Understanding how different cell types interact spatially within tissue microenvironments is critical for deciphering immune dynamics, tumor progression, and tissue organization. Many current spatial analysis methods assume symmetric associations or compute image-level summaries separately without sharing information across patients and cohorts , limiting biological interpretability and statistical power.

*Corresponding author: joelne@umich.edu. Present address: Department of Biomedical Engineering, Johns Hopkins University, Baltimore, MD, USA.

Results: We present SHADE (Spatial Hierarchical Asymmetry via Directional Estimation), a multilevel Bayesian framework for modeling asymmetric spatial interactions across scales. SHADE quantifies direction-specific cell-cell associations using smooth spatial interaction curves (SICs) and integrates data across tissue sections, patients, and cohorts. Through simulation studies, SHADE demonstrates improved accuracy, robustness, and interpretability over existing methods. Application to colorectal cancer multiplexed imaging data reveals distinct patterns of spatial asymmetry in immune and stromal organization, demonstrating SHADE's utility for characterizing directional spatial interactions in tissue microenvironments.

Availability and Implementation: Open-source implementation is available at `https://github.com/jeliason/SHADE` and `https://github.com/jeliason/shade_paper_code`, developed in R and Stan.

Keywords: spatial statistics, cell-cell interactions, Bayesian modeling, tissue microenvironment, multiplex imaging, colorectal cancer

Author Summary

The spatial arrangement of cells within tumors provides critical insights into cancer progression and treatment response. Modern imaging technologies can map cellular neighborhoods across multiple tissue sections from many patients, but almost all existing statistical methods face at least one of two key limitations: they assume spatial relationships are symmetric (if immune cells cluster near tumor cells, tumor cells must cluster near immune cells), and/or they analyze each tissue section independently rather than pooling information across the biological hierarchy. We developed SHADE (Spatial Hierarchical Asymmetry via Directional Estimation) to address both challenges simultaneously. SHADE captures directional spatial dependencies, allowing asymmetric relationships between cell types, while operating within a multilevel Bayesian framework that borrows strength across tissue sections, patients, and patient groups. This hierarchical structure yields more precise estimates and directly quan-

tifies variability at each biological scale. Applying SHADE to colorectal cancer data revealed distinct directional spatial patterns distinguishing immune-infiltrated from immune-excluded tumors, with substantial patient-level heterogeneity indicating diverse microenvironment architectures within disease subtypes. SHADE provides a principled approach for analyzing the directional, multi-scale organization of tissue microenvironments.

1 Introduction

Spatial dependencies between cell types play a central role in immune dynamics, tumor behavior, and tissue organization, motivating statistical models that can capture such interactions [Yuan, 2016, Maley et al., 2017]. The tumor microenvironment (TME) is a spatially structured system where cell arrangements are closely linked to disease progression and treatment response [Binnewies et al., 2018, Schürch et al., 2020]. Notably, these spatial interactions are frequently asymmetric: immune cells may cluster near tumor cells without the reverse being true, reflecting directional dependencies in tissue organization [Bindea et al., 2013].

Recent advances in multiplexed imaging technologies, including multiplexed immunofluorescence (mIF) and other high-resolution spatial profiling methods, have made it possible to quantify cell type spatial distributions and interactions within the tumor microenvironment at single-cell resolution [Sheng et al., 2023]. Standard pipelines for analyzing spatial cellular interactions in multiplexed imaging data typically compute second-order summary statistics, such as Ripley's K- and L-functions or the G-cross function, independently for each image to quantify tumor–immune interactions, infiltration patterns, or neighborhood structure [Barua et al., 2018, Vu et al., 2022, Canete et al., 2022, Samorodnitsky et al., 2024, Seal et al., 2024, Jing et al., 2025, Janeiro et al., 2024, Soupir et al., 2025]. These per-image summaries are then compared across groups or used as covariates in downstream analyses. Although effective for descriptive comparisons, this approach treats each image as

an isolated point pattern and cannot share information across biological replicates during estimation. Hierarchical models for replicated point patterns have been proposed [Bagchi and Illian, 2015, Lee et al., 2017, Myllymäki et al., 2014, Bell and Grunwald, 2004, Illian and Hendrichsen, 2010, Wrobel et al., 2024], but they typically model derived summaries via two-stage estimation or use parametric models fit via pseudolikelihood with random effects, rather than jointly estimating flexible interaction functions through full Bayesian multilevel inference at the point-process level.

Beyond these methodological limitations in handling replication, existing spatial models also struggle with directional dependencies. Gibbs point process models provide a flexible probabilistic framework [Moller and Waagepetersen, 2003, Baddeley et al., 2015], yet standard formulations assume symmetric interactions. While so-called hierarchical Gibbs models have been proposed to accommodate directionality [Högmander and Särkkä, 1999, Grabarnik and Särkkä, 2009], standard implementations depend on parametric interaction functions that impose restrictive assumptions. Observations based on the G-cross function suggest that spatial interactions between cell types are inherently asymmetric [Tsang et al., 2024], motivating statistical models that directly account for directional spatial effects.

In this work, we develop SHADE (Spatial Hierarchical Asymmetry via Directional Estimation), a statistical framework for modeling asymmetric spatial associations in tissue microenvironments. Our approach extends multitype Gibbs point process models [Baddeley et al., 2015, Moller and Waagepetersen, 2003, Högmander and Särkkä, 1999] by modeling directional associations via *spatial interaction curves (SICs)* that quantify how the presence of one cell type affects the expected density of another using flexible basis expansions within a multilevel Bayesian structure. The hierarchical framework enables partial pooling across biological scales (images, patients, cohorts) with full posterior inference for uncertainty quantification and heterogeneity analysis (Section 4.3). For computational efficiency, we use logistic regression with quadrature-based dummy points rather than direct Poisson likelihood estimation [Baddeley et al., 2014]. Technical comparison with Gibbs models is

provided in Supplement Section 1. An overview of the SHADE workflow is provided in Figure 1.

2 Methods

2.1 Multilevel Modeling of Conditional Spatial Point Processes

We model the spatial distribution of a target cell type B given the presence of one or more conditioning cell types $A_1, A_2, \ldots, A_K$, using a hierarchical framework based on conditional spatial point processes. Our approach extends hierarchical Gibbs models [Högmander and Särkkä, 1999, Grabarnik and Särkkä, 2009] and is designed to flexibly estimate asymmetric spatial association patterns while accounting for multilevel variation across images, patients, and cohorts.

Let $X_{A_k}, X_B \subset W$ denote the observed spatial point patterns of cell types A_k and B, respectively, within a two-dimensional tissue region $W \subset \mathbb{R}^2$. Formally, $X_{A_k} = \{x_i^{(k)} \in W \mid i = 1, \ldots, N_{A_k}\}$, $X_B = \{y_j \in W \mid j = 1, \ldots, N_B\}$, where $x_i^{(k)} = (x_{i1}^{(k)}, x_{i2}^{(k)}) \in \mathbb{R}^2$ denotes the two-dimensional spatial coordinate of the i-th cell of type A_k, and $y_j = (y_{j1}, y_{j2}) \in \mathbb{R}^2$ denotes the coordinate of the j-th cell of type B. The quantities N_{A_k} and N_B indicate the total number of observed cells of type A_k and B, respectively. The observation window W corresponds to the region of tissue captured in the image, typically a rectangular subset of the plane defined by the image dimensions.

In practice, X_{A_k} and X_B are obtained from image segmentation and cell type classification pipelines applied to high-resolution tissue images, such as those generated by multiplexed imaging platforms.

We model the spatial distribution of X_B (the *target* cell type, e.g., immune cells) conditional on $X_{A_1}, \ldots, X_{A_K}$ (the *source* cell types, e.g., tumor cells and vasculature) by assuming that $X_B \mid X_{A_1}, \ldots, X_{A_K}$ follows an inhomogeneous Poisson point process [Baddeley et al., 2015]. This allows the expected density of target cells to vary flexibly across space as a

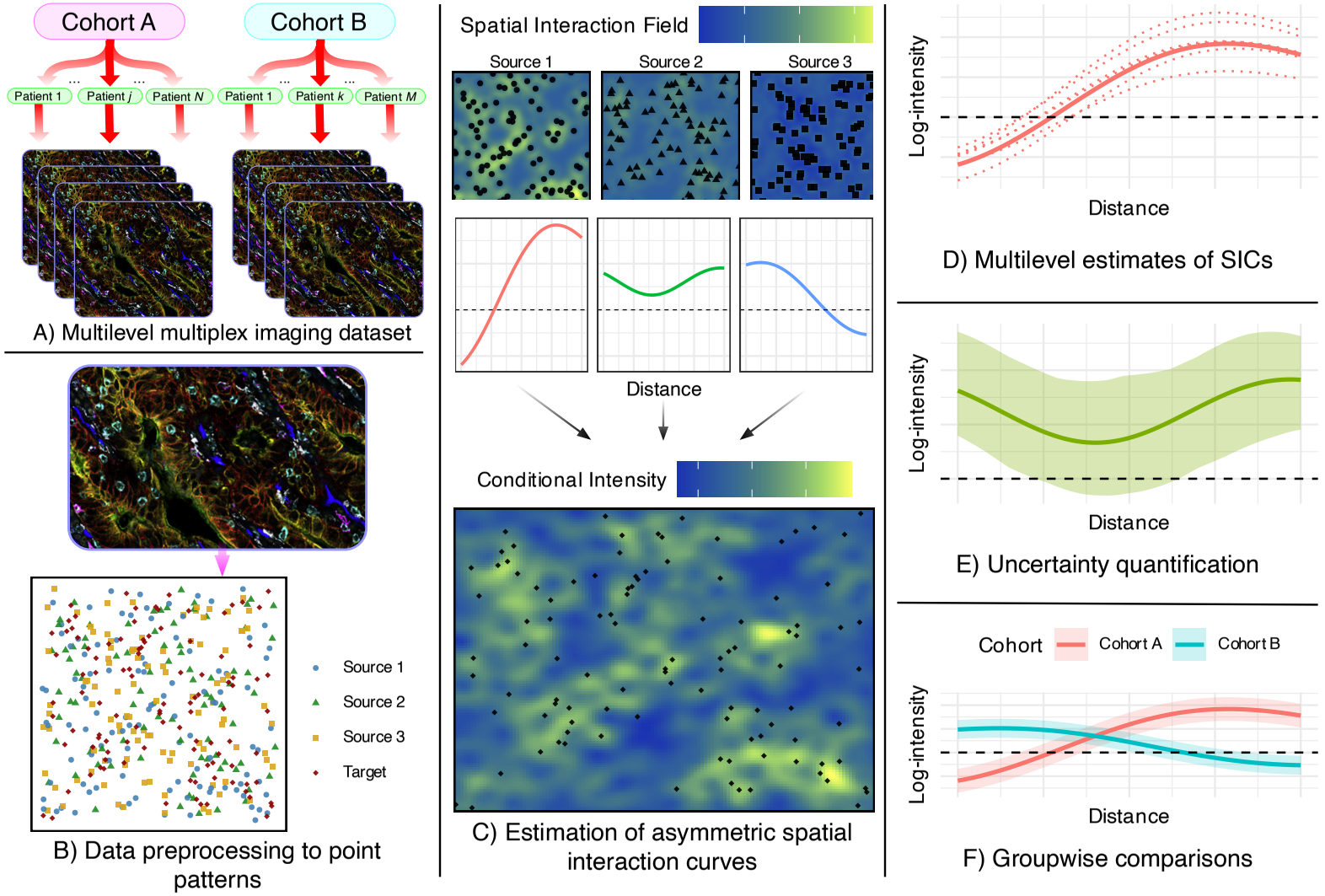

Figure 1: Summary of the SHADE (Spatial Hierarchical Asymmetry via Directional Estimation) framework. **A)** Multiplexed imaging data is structured hierarchically across cohorts, patients, and images. Multiplex images were adapted from Schürch et al. [2020] and are used under a Creative Commons CC BY 4.0 license. **B)** Images are processed into spatial point patterns with cell type annotations. **C)** SHADE estimates Spatial Interaction Curves (SICs) that capture directional associations between cell types across spatial scales. **D)** SICs are estimated at cohort, patient, and image levels, enabling multilevel analysis of spatial heterogeneity. **E)** Posterior distributions provide uncertainty quantification. **F)** SICs can be compared across cohorts to assess differences in spatial organization.

function of source cell locations and covariates, enabling the framework to represent complex spatial patterns including clustering, repulsion, and distance-dependent associations. While alternative models exist (e.g., Cox processes, cluster processes, Gibbs processes), the inhomogeneous Poisson process provides the best balance of flexibility, interpretability, and computational feasibility for our application [Baddeley et al., 2015]. The likelihood is:

$$L(X_B \mid X_{A_1}, \ldots, X_{A_K}) = \left[\prod_{v \in X_B} \lambda(v \mid X_{A_1}, \ldots, X_{A_K}) \right] \times \exp\left(- \int_W \lambda(v \mid X_{A_1}, \ldots, X_{A_K})\, dv \right), \tag{1}$$

where the product runs over all observed locations of type B, while the integral accounts for the total expected intensity over the observation window W. The point process for X_B is entirely characterized by its *conditional intensity function* $\lambda(v \mid X_{A_1}, \ldots, X_{A_K})$, which defines the expected local density of type B cells at any location $v \in W$, conditioned on the spatial configurations of the conditioning cell types, that is, $\lambda(v \mid X_{A_1}, \ldots, X_{A_K}) = \lim_{|dv| \to 0} \frac{1}{|dv|} E[N_B(dv) \mid X_{A_1}, \ldots, X_{A_K}]$.

We model $\lambda(\cdot)$ as depending log-linearly on the observed patterns of $A_1, \ldots, A_K$ cells:

$$\log \lambda(v \mid X_{A_1}, \ldots, X_{A_K}) = \beta_0 + \boldsymbol{z}^\top(v)\boldsymbol{\beta} + \sum_{k=1}^{K} \boldsymbol{q}_{A_k}^\top(v)\boldsymbol{\psi}_{A_k} \tag{2}$$

In (2), the term $\boldsymbol{z}(v) \in \mathbb{R}^J$ is a vector of covariates at location v (including an intercept), with corresponding coefficients $\boldsymbol{\beta} \in \mathbb{R}^J$. The vector $\boldsymbol{q}_{A_k}(v) \in \mathbb{R}^P$ encodes spatial interaction features between type A_k and type B; its p-th element is defined as:

$$[\boldsymbol{q}_{A_k}(v)]_p = \sum_{x \in X_{A_k}} \phi_p\left(\operatorname{dist}(v, x)\right), \tag{3}$$

where $\phi_p(\cdot)$ is a basis function (e.g., a B-spline or Gaussian kernel) that modulates the influence of a type A_k cell at a given distance from v and $\boldsymbol{\psi}_{A_k} \in \mathbb{R}^P$ are the corresponding coefficients. Finally, the intercept term (β_0) captures baseline log-intensity, effectively nor-

malizing to average target cell density. SIC values then quantify deviations from this baseline as a function of proximity to source cells, ensuring curves are directly comparable across images and patients despite differences in overall cell abundance. This formulation flexibly captures how proximity to different cell types influences the expected density of type B cells across spatial scales. Our use of smooth interaction features in (3) reflects biologically realistic, distance-dependent associations. In doing so, we generalize traditional Gibbs process formulations by avoiding rigid parametric forms such as fixed interaction radii [Grabarnik and Särkkä, 2009], which fail to capture the continuous and often subtle variations observed in biological spatial interactions [Baddeley and Turner, 2005].

While the model specified in (2) provides a flexible representation of spatial interactions through basis expansions, directly interpreting the estimated coefficients $\boldsymbol{\psi}_{A_k}$ can be difficult. In particular, biological interest often centers on how the strength and direction of association between a conditioning cell type A_k and a target cell type B vary as a function of distance. To facilitate interpretable biological insights, we next define a derived quantity, the *spatial interaction curve* (SIC), which summarizes the estimated effect of proximity to A_k cells on the expected density of B cells across spatial scales.

2.1.1 Spatial Interaction Curve

The SIC summarizes the asymmetric spatial association between a conditioning cell type A_k and a target cell type B as a function of distance s:

$$\mathrm{SIC}_{A_k \to B}(s) = \sum_{p=1}^{P} \psi_{A_k}^{(p)} \phi_p(s), \tag{4}$$

This curve represents the expected contribution of type A_k cells to the log-intensity of type B cells as a function of distance s from a type A_k cell. Here, log-intensity refers to the logarithm of the conditional intensity function $\lambda(v)$ (Equation 2), which describes the expected spatial density of type B cells (in cells per unit area) at any location v. Because the model is log-

linear, SIC values quantify additive changes on the log-intensity scale, which correspond to multiplicative changes in actual cell density. For example, SIC $= 0.2$ at distance s implies an $e^{0.2} \approx 1.22\times$ (or 22%) increase in the expected local density of type B cells at radius s from a type A_k cell, while SIC $= -0.3$ corresponds to an $e^{-0.3} \approx 0.74\times$ decrease (26% reduction). Figure 2 illustrates how SIC values correspond to spatial attraction (positive) or repulsion (negative).

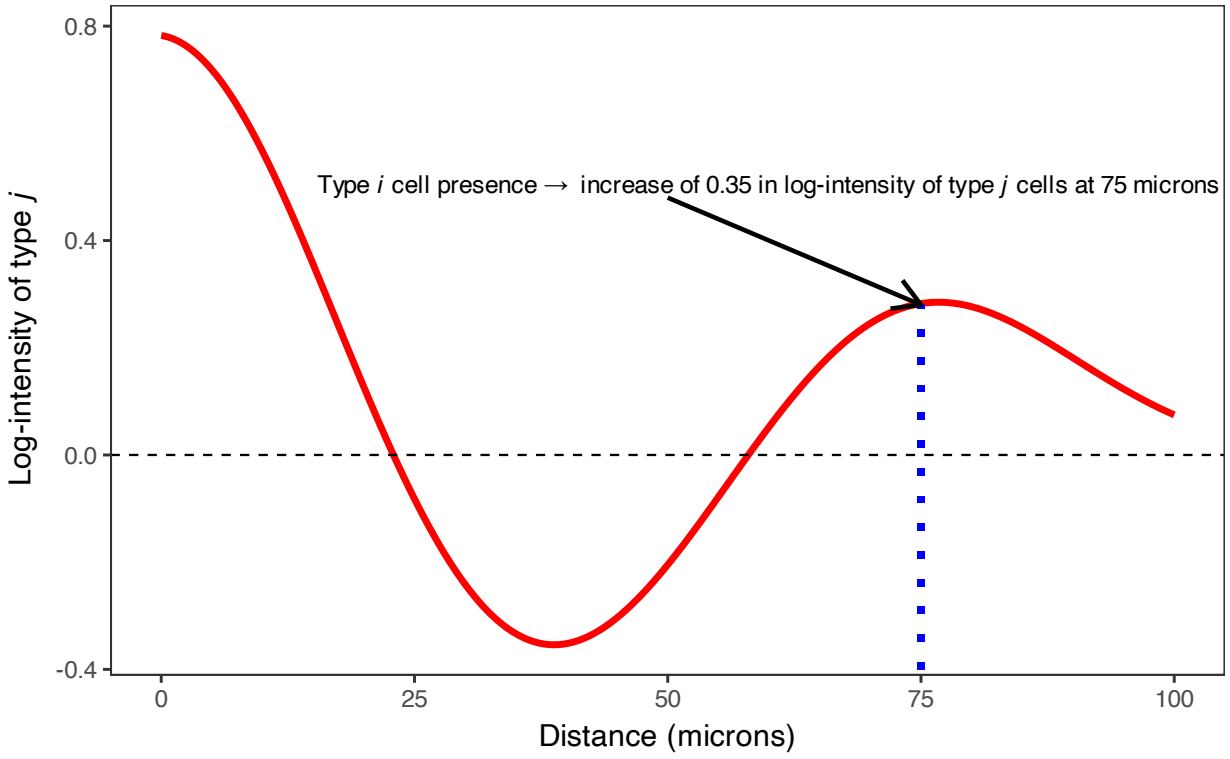

Figure 2: An example spatial interaction curve showing the effect of a source cell type A_k on a target cell type B. At each distance s, the curve value represents the change in log-intensity of type B associated with the presence of a type A_k cell at distance s.

A key advantage of our framework is that the spatial interaction terms $\boldsymbol{\psi}_{A_k}$ can take both positive and negative values, allowing for flexible modeling of attraction and repulsion. This mirrors the flexibility of hierarchical Gibbs models while overcoming constraints in symmetric pairwise interaction models, which typically restrict interaction terms to be non-positive and therefore cannot directly model spatial attraction.

Because cell centroids cannot occur arbitrarily close in space, very short distances (below

approximately 1-2 cell diameters) can reflect geometric crowding, cell-cell contact, or segmentation artifacts, making biological interpretation ambiguous. We therefore predefine a minimum interaction radius $r_{\min} = 25$ μm (approximately 1.5-2 typical cell diameters) and report spatial interaction curves only for $r \geq r_{\min}$. The model is fit using all observed cell locations, but posterior summaries and spatial interaction curves are evaluated and reported only at distances $r \geq r_{\min}$ to focus interpretation on unambiguous intercellular spacing. All band-level posterior probabilities are computed on intervals $I \subseteq [r_{\min}, \infty)$.

2.1.2 Interpreting Spatial Interaction Curves

Our modeling framework captures *predictive* spatial associations, not biological causation. A strong $A \to B$ SIC indicates that type A cell locations are statistically predictive of local type B density, formally meaning that the conditional intensity $\lambda(v \mid X_A)$ differs from the marginal intensity $\lambda_B(v)$. While SICs quantify the strength and direction of spatial predictability, they do not establish causal biological effects. The model can incorporate spatial covariates (e.g., distance to tumor margin) to adjust for confounding from first-order intensity effects.

2.2 Multilevel Bayesian Model

To capture biological variability across individuals and sampling levels, we impose a hierarchical prior structure on the spatial interaction coefficients. For each conditioning cell type A_k, the interaction coefficients are indexed hierarchically across three levels: cohort (ψ), patient (γ), and image (δ). Specifically, for each basis function p, we define:

$$\begin{aligned} \psi_{A_k}^{(g,p)} &\sim \mathcal{N}(0, \sigma^2_{\text{cohort}}), \\ \gamma_{A_k}^{(n,p)} &\sim \mathcal{N}(\psi_{A_k}^{(g(n),p)}, \sigma^2_{\text{patient}}), \\ \delta_{A_k}^{(m,p)} &\sim \mathcal{N}(\gamma_{A_k}^{(n(m),p)}, \sigma^2_{\text{image}}), \end{aligned} \tag{5}$$

where $g(n)$ maps patient n to its cohort, and $n(m)$ maps image m to its corresponding

patient. Each image-level coefficient $\delta_{A_k}^{(m,p)}$ governs the localized effect of source cell type A_k on target cell type B at distance scale p, within image m.

This hierarchical formulation enables partial pooling across the dataset structure, improving estimation stability while preserving biologically meaningful heterogeneity in spatial interactions. By modeling variation at the cohort, patient, and image levels, the framework supports inference on both shared and context-specific spatial association patterns. When comparing spatial organization across biological groups (e.g., treatment responders vs. non-responders, different tumor subtypes), each group is modeled as a separate cohort with its own cohort-level parameters $\psi_{A_k}^{(g,p)}$. Differences between groups are then assessed by comparing the posterior distributions of these cohort-level parameters, as quantified through SICs (Equation 4) and their associated simultaneous credible bands.

Hyperpriors for the variance components σ^2_{cohort}, $\sigma^2_{\text{patient}}$, and σ^2_{image} are detailed in the Supplement.

2.3 Uncertainty Quantification and Prioritization of Cell Type Pairs

To quantify uncertainty in estimated SICs and assess statistical significance, we employ simultaneous 95% credible bands that account for multiple comparisons across the distance domain. Unlike pointwise credible intervals, simultaneous bands provide joint coverage across all distances within a specified range, offering stronger protection against false discoveries. Statistical significance can be assessed by examining whether the simultaneous band excludes zero over a distance range of interest. Full implementation details are provided in the Supplement (Section 4.1).

In exploratory analyses involving many cell type pairs ($K(K-1)$ directed pairs for K cell types), we propose summary measures to facilitate prioritization: peak location and magnitude (identifying where the strongest interaction occurs), persistence over biologically relevant distance ranges (quantifying consistent associations within pre-specified intervals), and

overall strength (integrating absolute effect sizes over significant regions). These measures can be computed across all source–target pairs and visualized as heatmaps for systematic comparison. Formal definitions are provided in the Supplement (Section 4.2).

2.4 Logistic Regression Approximation for Computational Efficiency

Direct estimation of the Poisson likelihood in spatial point process models requires numerical integration over fine spatial grids, which becomes computationally expensive and unstable. Following Baddeley et al. [2014], we use a logistic regression approximation that introduces dummy points sampled from a homogeneous Poisson process, reframing spatial intensity estimation as binary classification. This approach avoids computational challenges such as singular design matrices and biased uncertainty estimates that arise in direct Poisson modeling. Importantly, this approximation does not require the target cell process to be homogeneous—only the dummy/quadrature points are placed homogeneously for computational convenience. Target cells are still modeled as an inhomogeneous Poisson process via the conditional intensity $\lambda(v)$, with spatial variation captured through distance-based SIC features $\boldsymbol{q}_{A_k}(v)$ and optional spatial covariates $\boldsymbol{z}(v)$ (Equation 2). While our later analysis does not explicitly model compartmental variation in baseline rates, the SIC features already capture local variation driven by proximity to different cell types. The framework is extensible to include compartment indicators or other spatially-varying features as additional covariates if discrete tissue domains are suspected to drive baseline intensity differences independent of cell-cell interactions. Details of the approximation are provided in Supplement Section 2.

2.5 Model Estimation and Computational Implementation

Model fitting is implemented in `Stan` using Hamiltonian Monte Carlo (HMC) via `cmdstanr` [Stan Development Team, 2024, Gabry et al., 2024].

To approximate the likelihood, we first generate a set of dummy points D from a homogeneous Poisson process with intensity λ_{dummy} over the observation window W. For each location $v \in X_B \cup D$, we then compute spatial covariates $\boldsymbol{z}(v)$ and interaction features $\boldsymbol{q}_{A_k}(v)$, where each interaction feature encodes basis-function-weighted distances to cells of type A_k.

Feature construction for each focal cell type B involves evaluating inter-cell distances between observed and dummy focal locations and all non-focal cells. This step scales as $\mathcal{O}(n_{\text{focal}} \times n_{\text{source}})$, which is quadratic in the total number of cells when the focal and source sets are of similar size. However, this operation is implemented using the optimized `crossdist` routine from `spatstat.geom`, which efficiently computes pairwise distances in compiled code. The resulting distance matrix is reused across all basis functions $\{\phi_p\}$ and source types $\{A_k\}$, so the dominant cost occurs only once per focal type.

To assess the practical runtime implications, we performed a timing experiment varying the total number of cells from 5,000 to 250,000 using variational inference (Supplement, Section 4.8). Feature construction time scaled as $O(n^{1.46})$ (empirical exponent from log-log regression), while total model fitting time scaled as $O(n^{0.85})$ due to efficient distance matrix reuse. At 100,000 cells, total fitting time was approximately 36 seconds; at 250,000 cells, approximately 133 seconds. These benchmarks demonstrate that SHADE remains computationally tractable for large-scale multiplexed imaging studies.

Using these constructed features, we fit a multilevel Bayesian logistic regression model based on the approximation in (10), with spatial interaction coefficients $\boldsymbol{\delta}_{A_k}^{(m,p)}$ modeled hierarchically according to the priors in (5). Finally, we extract posterior draws of the interaction coefficients and reconstruct the spatial interaction curves using (4).

3 Simulation Studies

To evaluate SHADE's performance, we conducted simulation studies generating synthetic spatial point patterns with asymmetric interactions and multilevel structure. Spatial patterns were simulated within a bounded domain $W = [0, S] \times [0, S]$, with source points from a homogeneous Poisson process and target points influenced by spatial interaction curves defined over source-target distances. Hierarchical structure was introduced via interaction coefficients generated according to (5).

The final point pattern was converted into a logistic regression dataset using dummy points sampled from a homogeneous Poisson process with intensity λ_{dummy}, and spatial interaction features were computed as in (3). We first validated that SHADE's hierarchical structure substantially improves estimation quality compared to non-hierarchical alternatives (Supplement Section 4.4). We then conducted a comprehensive comparison of SHADE's detection capabilities against established spatial analysis methods across varying data conditions, presented below. Additional hyperparameter studies are provided in Supplement Section 4.5.

3.1 Comparison of spatial pattern detection accuracy across methods

We evaluated SHADE's detection power and calibration against established spatial analysis methods by generating hierarchical spatial point patterns with known positive spatial interactions between two cell types, modeling a single patient cohort with attraction patterns across multiple distance scales.

These simulations focus on *image-level* detection capabilities—the ability to identify spatial interactions within individual tissue sections using envelope-based methods. While SHADE's hierarchical framework enables inference at multiple biological scales (image, patient, and cohort levels), we compare here against G-cross and K-cross envelope tests that assess significance via completely spatially random (CSR) Monte Carlo simulations. In Section 5.5.3, we present a complementary analysis comparing SHADE's group-level inference

with functional data analysis methods that analyze marginal pairwise summary statistics.

We simulated a single cohort of spatial point patterns with patient- and image-level hierarchical structure (40 patients, 1–3 images per patient) using radial basis functions to model positive spatial interactions at short-, medium-, and long-range scales. We varied source cell density (the conditioning cell type: 15 vs. 150 cells per image) and target cell density (the cell type being modeled: 15 vs. 150 cells per image) across 50 replicates per condition. This design allows assessment of how SHADE's hierarchical pooling performs when the conditioning information is sparse versus abundant, and when multiple images per patient are available for information sharing. Detection power was evaluated as the proportion of simulations in which the method correctly identified that the spatial interaction curve differs from zero anywhere in the 0–75 μm range. For SHADE, detection was based on whether 95% simultaneous credible bands (see Supplement, Section 4.1) excluded zero at any distance. For comparison, we evaluated three baseline approaches: (1) G-cross envelope tests [Baddeley et al., 2015], testing whether the observed nearest-neighbor distribution falls outside 95% global envelopes constructed from 99 completely spatially random (CSR) simulations; (2) K-cross (specifically, L-cross) envelope tests, using cumulative counts rather than nearest-neighbor distances; and (3) a 'Flat' model that estimates SICs independently for each image without hierarchical pooling. Type I error rates were assessed using null simulations with zero spatial interactions. Figure 3 illustrates one simulated example; full simulation details are provided in the Supplement.

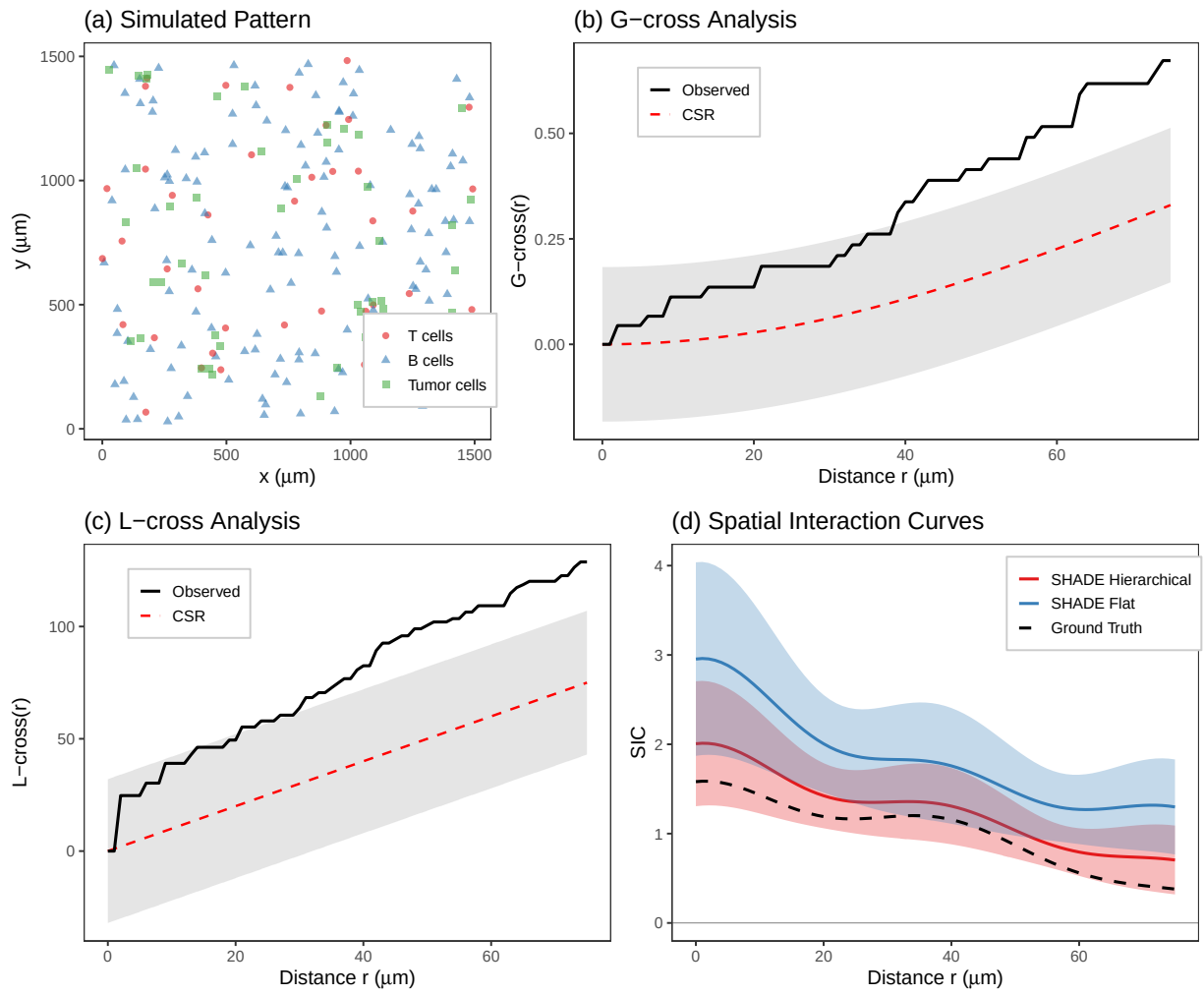

Figure 3: Simulation study comparing spatial analysis methods. (a) Simulated pattern showing T cells, B cells, and tumor cells in a 1500×1500 μm^2 region with known spatial clustering. (b) G-cross analysis with the observed curve (black), CSR expectation (dashed red), and 95% global envelope (gray ribbon) from 99 CSR simulations. (c) L-cross analysis, which counts all tumor cells within distance r of a typical T cell rather than measuring nearest-neighbor distances. (d) SIC estimates from SHADE Hierarchical (red), SHADE Flat (blue), and the ground truth (black dashed), with simultaneous 95% credible bands.

Figure 4 shows detection power across simulation conditions, where power is defined as the proportion of simulated datasets in which the method correctly identifies that the spatial interaction curve differs from zero. Results reveal that SHADE Hierarchical's performance depends critically on two factors: source cell density (which provides conditioning information) and the number of images available for hierarchical pooling.

First, when source density is high (regardless of target density), SHADE achieves excellent median power (100%) across all conditions, substantially outperforming envelope tests when target density is low (SHADE 100% vs. G-cross 77%, K-cross 73%). Abundant source cells provide strong conditioning information that hierarchical pooling can effectively leverage. Conversely, when source density is low, performance depends on whether multiple images are available: with 2–3 images per patient, median power reaches 100%; with only 1 image, power drops to 31% as limited conditioning information per image prevents effective pooling.

Next, we found that SHADE Hierarchical requires at least 2 images per patient for stable performance. With only 1 image per patient, the method exhibits extreme behavior: overly conservative under some conditions (100% coverage, 0% type I error when target density is high and source density is low) and unreliable under others (0% power with high type I error variability when both densities are low). With 2–3 images, performance stabilizes substantially, achieving high power when source density is adequate while maintaining reasonable calibration.

When both source and target densities are low, all methods struggle. With 2–3 images per patient, SHADE achieves 26–28% median power with 94% coverage and well-controlled type I error (4%), demonstrating appropriate conservatism (SHADE Flat has higher power but much worse coverage in this regime, in the multi-image case - see Supplementary Figure S11). Interestingly, G-cross performs best in this regime (49% power).

Coverage and type I error performance (Supplement Section 4.9) reveal adaptive calibration. When source density is high (favorable for detection), SHADE trades calibration for sensitivity (55% coverage, 100% power, <1% type I error). When both densities are low (unfavorable for detection), SHADE becomes appropriately conservative (94% coverage, 28% power, 4% type I error). This contrasts with SHADE Flat, which maintains poor coverage (73%) regardless of scenario and shows severely inflated type I error rates (28%). Median type I error rates for SHADE Hierarchical with 2–3 images are well-controlled (0.8–7.5%), comparable to envelope tests (G-cross: 2.5–8.8%; K-cross: 1.3–6.7%), though with

higher variability (IQR up to 0.12), indicating occasional liberal inference under challenging conditions.

3.1.1 Robustness to spatial confounding.

We also tested SHADE's performance when the model is misspecified due to unmeasured spatial heterogeneity—specifically, discrete tissue compartments (e.g., tumor islands, stromal regions) that create baseline density differences independent of source-target interactions (Figure 5; Supplement Section 4.10). Results reveal regime-dependent bias: when both cell types are abundant, SHADE achieves perfect detection power but exhibits elevated Type I error rates (11.7–17.1%) and severely undercovers (43–52% vs. expected 95%), incorrectly attributing compartment effects to source-target interactions. When target density is low, wider credible bands provide partial robustness (82–93% coverage, 1.7–5.8% Type I error). These findings indicate that unmeasured spatial structure can produce substantial bias in high-density scenarios, suggesting the need for explicit compartment modeling or sensitivity analyses when such heterogeneity is suspected.

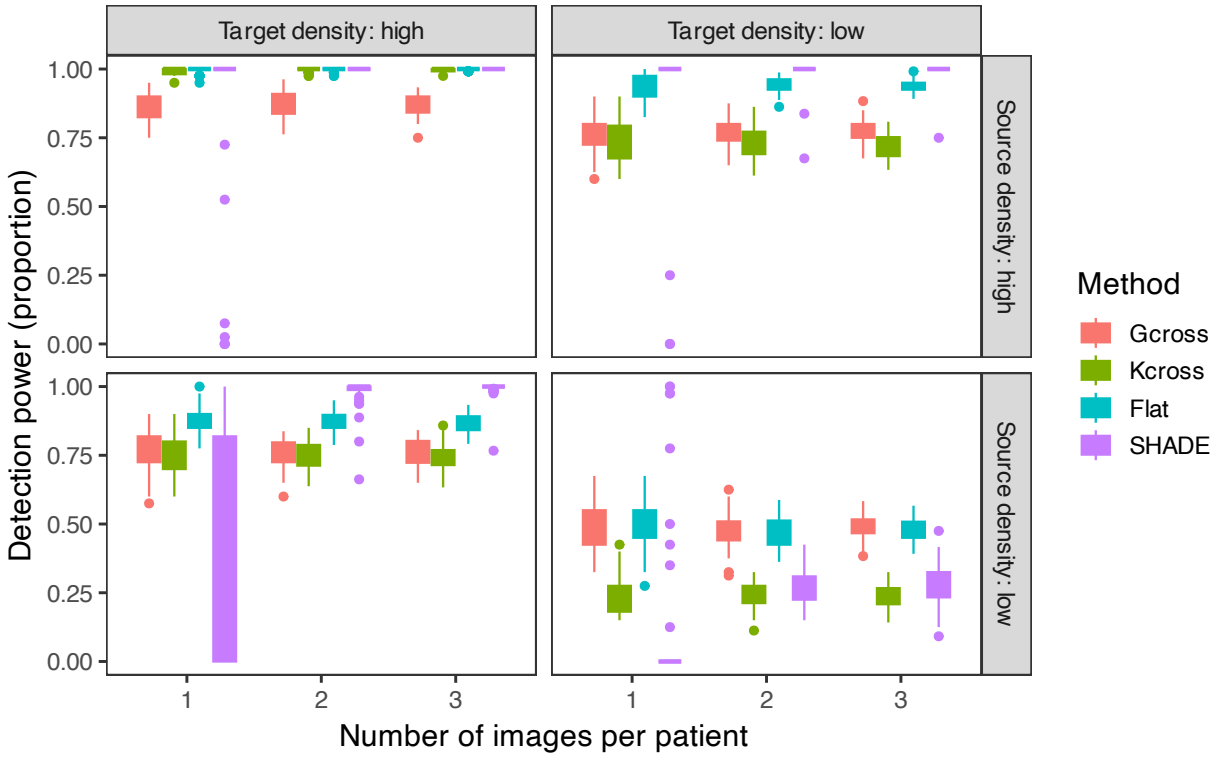

Figure 4: Detection power comparison across simulation conditions. Boxplots show the proportion of datasets in which methods correctly identify non-zero spatial interactions by testing whether simultaneous credible bands (SHADE) or global envelopes (G-cross, K-cross) exclude zero anywhere in the 0–75 μm range. Results are stratified by source cell density (rows: the conditioning cell type) and target cell density (columns: the cell type being modeled), with number of images per patient (1, 2, or 3) shown on the x-axis. SHADE Hierarchical achieves highest power when source density is high, with performance when source density is low depending critically on having multiple images per patient available for hierarchical pooling (see main text).

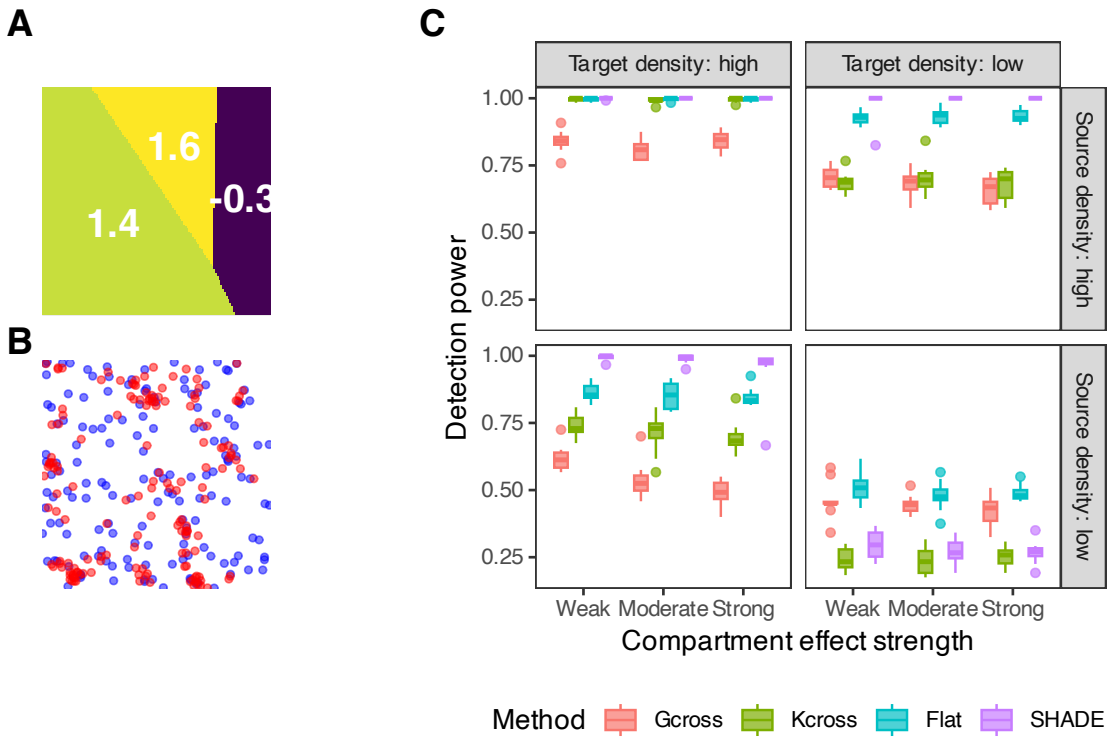

Figure 5: Robustness to spatial confounding via compartments. A: Compartment structure showing log-intensity effect on target density (3 compartments with moderate effect strength = 1.2). B: Example simulated pattern with tumor cells (red) and T cells (blue). C: Detection power stratified by compartment effect strength (weak/moderate/strong), source density (T cells, rows), and target density (tumor cells, columns). Despite unmeasured compartments, all methods maintain high power in favorable scenarios. However, elevated Type I error rates (see Supplement Section 4.10) indicate that SHADE incorrectly attributes compartment effects to source-target interactions when both cell types are abundant, demonstrating regime-dependent confounding bias.

4 Results: Multiscale inference of directional spatial interactions in colorectal cancer

4.1 Description of colorectal cancer dataset

We applied SHADE to a publicly available colorectal cancer dataset of multiplexed tumor tissue images from 35 patients [Schürch et al., 2020], with four images per patient annotated at single-cell resolution across 16 cell types. Patients were stratified by immune pheno-

type: Crohn's-like reaction (CLR, immune-infiltrated) and diffuse inflammatory infiltration (DII, immune-excluded). We analyzed the eight most abundant cell types, reclassifying "stroma" and "smooth muscle" as hybrid epithelial-mesenchymal (E/M) cells and cancer-associated fibroblasts (CAFs) based on marker expression [Kuburich et al., 2024, Cao et al., 2025]. Target populations (CD8$^+$ T cells, memory CD4$^+$ T cells, granulocytes) were selected for relevance to anti-tumor immunity; source populations (vasculature, tumor cells, CAFs, tumor-associated macrophages, hybrid E/M cells) represent key tissue architecture and immune regulatory elements. For each target type, we jointly estimated SICs with respect to all sources (data preparation details in Supplement Section 5.1).

4.2 How are specific cell types spatially organized in the tumor microenvironment?

A core question in tumor microenvironment analysis is whether certain cell types tend to cluster near or avoid others, and how these patterns vary with spatial scale. Such spatial relationships reflect underlying mechanisms of attraction, repulsion, communication, or physical constraint, and may provide insight into processes like immune surveillance, tumor evasion, and niche formation. SHADE's directional SICs allow detection of cell-type-specific clustering and exclusion behaviors across scales.

We extracted image-, patient-, and cohort-level interaction parameters ($\delta^{(m,p)}_{t_1\to t_2}$, $\gamma^{(n,p)}_{t_1\to t_2}$, and $\psi^{(g,p)}_{t_1\to t_2}$) and computed SICs as in Equation 4. Figure 6 shows an example with cytotoxic T lymphocytes (CTLs, CD8$^+$ T cells) as the target cell type and CAFs as a source, highlighting differential organization between patient groups. At $\sim$75 μm, CTLs in CLR patients tend to cluster around CAFs (log-intensity > 0), whereas in DII patients, CTLs appear depleted near CAFs. Patient-level curves reveal substantial within-group heterogeneity.

Across all cell-type pairs, we observed consistent short-range ($<$25 μm) negative associations, likely reflecting physical crowding. At intermediate ranges (25–75 μm), many pairs showed a distinct positive peak, suggestive of clustering, often differing in magnitude be-

tween patient groups. Associations at longer distances (>75 μm) were generally weaker or absent, indicating limited spatial coordination at larger scales.

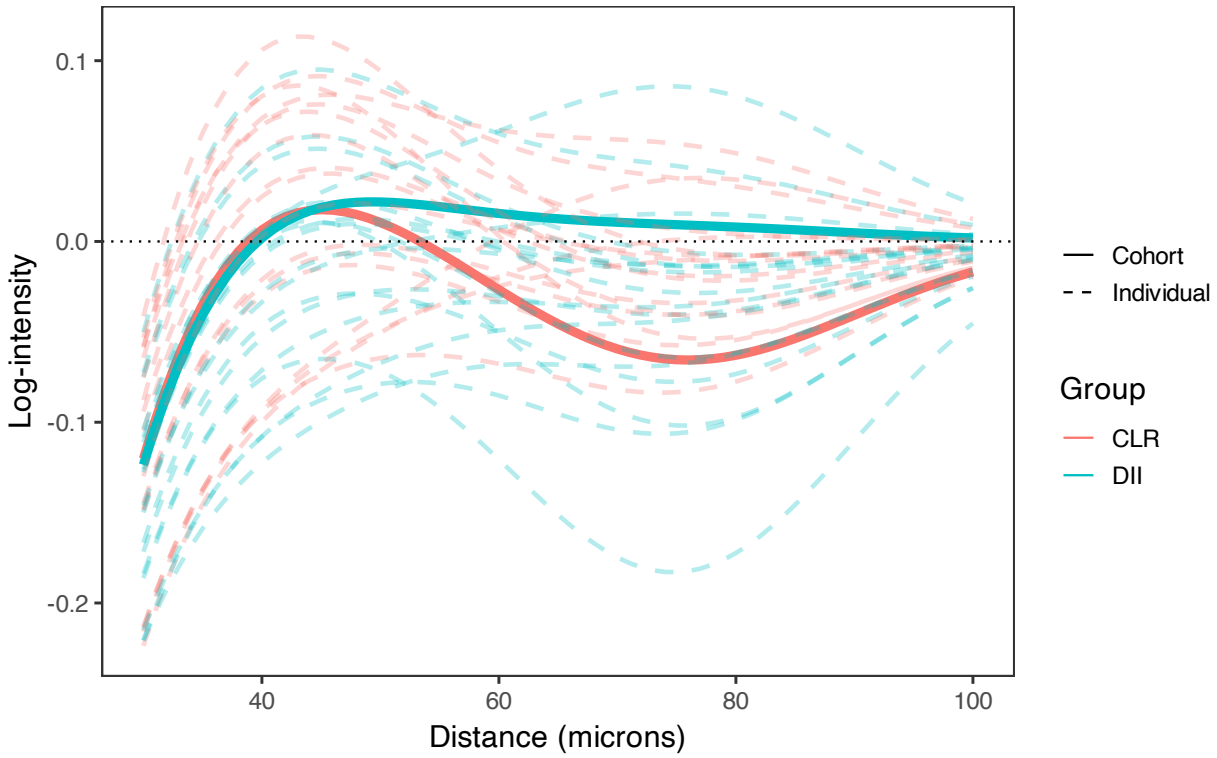

Figure 6: SIC showing the directional association of CAFs (source) with CTLs (target), stratified by patient group. Solid lines show cohort-level estimates for CLR and DII; dashed lines show patient-level SICs, illustrating hierarchical variability across patients within each cohort. CTLs in CLR patients exhibit midrange clustering around CAFs, while DII patients show neutral to avoidant patterns, indicating group-specific spatial organization.

4.3 How do spatial interaction patterns vary across patients and tissue sections?

Spatial interactions can vary across tumors and even between sections from the same patient, reflecting biologically meaningful heterogeneity in tumor architecture or immune organization. Unlike descriptive spatial statistics that compute separate summaries for each image, SHADE's hierarchical Bayesian model jointly estimates SICs at the image, patient, and cohort levels through partial pooling. This enables formal decomposition and quantification

of variability at each biological scale, allowing us to assess both intra- and inter-patient variability and distinguish conserved from patient-specific spatial patterns. Examples of patient-level and image-level SICs for cell type pairs exhibiting high within-patient heterogeneity are shown in Figure 7.

To assess variability in spatial interaction structure across samples, we summarize between-patient and between-image heterogeneity using median absolute deviation (MAD)-based estimates. These measures are defined in Supplement Section 7. We also examined heterogeneity in spatial interaction structure across patients and images. Comparing heterogeneity patterns between CLR and DII tumor subtypes reveals subtype-specific differences in variability (Figure 8). DII tumors exhibit greater heterogeneity for specific interactions (e.g., memory CD4+ T cells with tumor cells, granulocytes with vasculature), while CLR tumors show greater heterogeneity in granulocyte-stromal interactions (e.g., granulocyte-CAF, granulocyte-hybrid E/M). These patterns hold at both patient and image levels, demonstrating that tumor subtype affects not only mean spatial organization (Section 4.4) but also the variability of spatial interactions across biological scales.

4.4 How do immune and stromal spatial interactions differ between hot and cold tumors?

Distinct tumor immune phenotypes—such as immune-infiltrated versus immune-excluded tumors—are associated with differential immune activity and prognosis. These differences are often accompanied by changes in how immune and stromal cells are spatially arranged in relation to tumor cells and each other. We used SHADE to compare SICs across these patient groups and identify interactions that are enriched or depleted in each context. This allowed us to link differences in spatial structure to known functional differences in immune activity.

Figure 9 shows the estimated cohort-level SICs for all source-target cell type pairs, stratified by patient group. Comparing the CLR and DII curves reveals several notable differences

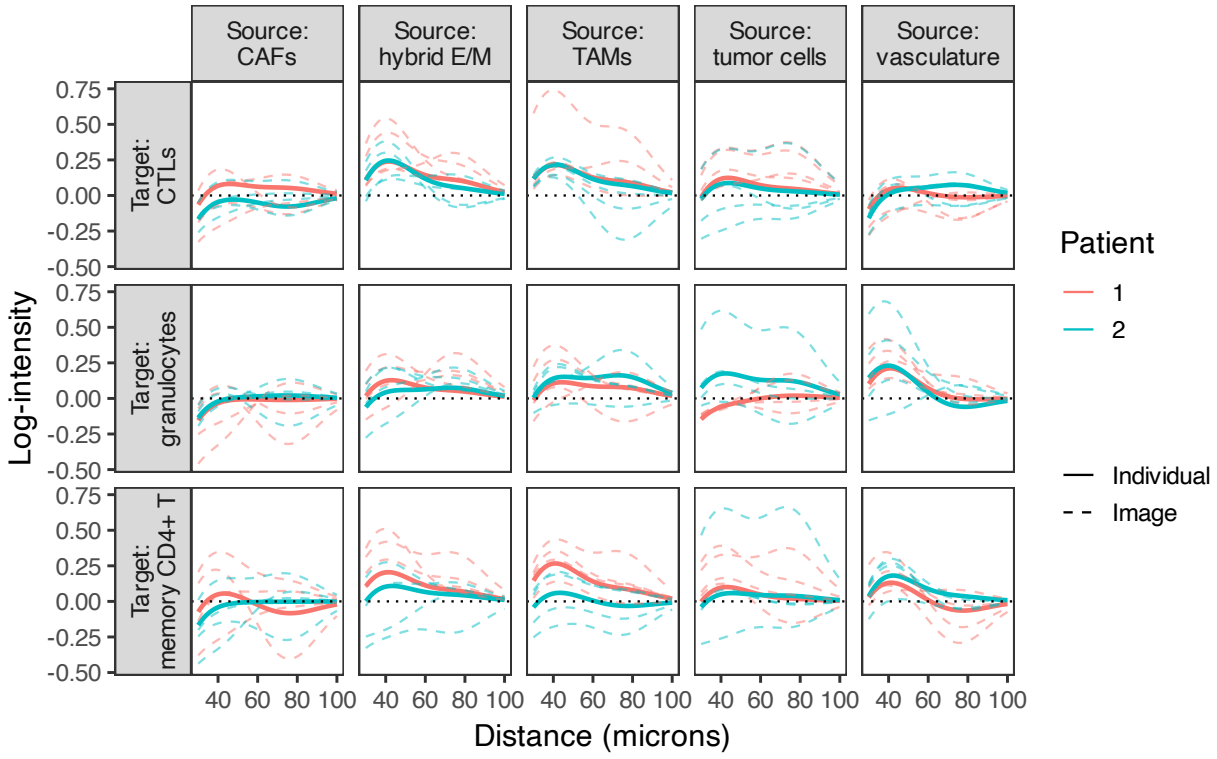

Figure 7: Examples of patient- and image-level SICs for cell type pairs with high within-patient MAD values. Solid lines show patient-level SICs; dotted lines show image-level SICs from individual tissue sections, illustrating hierarchical variability within patients.

in spatial interaction structure. While none of these differences reach statistical significance at the 95% credible level (i.e., simultaneous credible bands for the SICs overlap everywhere), we highlight several exploratory patterns that warrant validation in independent cohorts.

DII patients exhibited greater clustering of CTLs around tumor cells and greater granulocyte-TAM attraction, potentially reflecting distinct myeloid-lymphoid organization. In contrast, CLR patients showed stronger CTL attraction to hybrid E/M cells at short ranges and greater immune-stromal spatial segregation, with enhanced repulsion of CTLs and memory CD4+ T cells from CAFs and hybrid E/M cells at medium-to-long ranges. These hypothesis-generating observations suggest distinct spatial architectures in immune-infiltrated versus immune-excluded tumors (see Supplement Section 5.2 for detailed discussion and mechanistic interpretation).

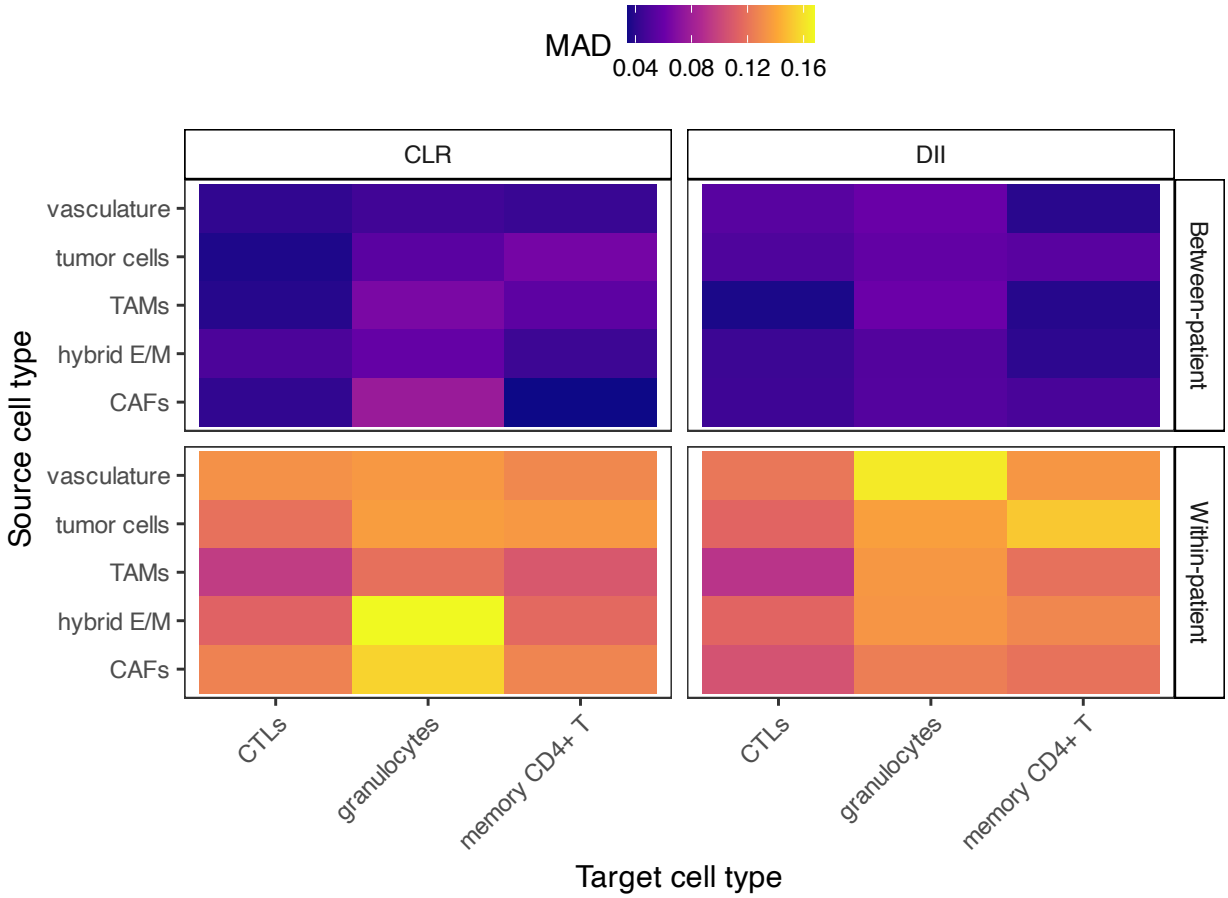

Figure 8: Heatmaps show median absolute deviation (MAD) of spatial interaction curve deviations as a measure of heterogeneity for 15 source-target cell type pairs. Top row: between-patient heterogeneity (MAD of patient-level deviations from cohort mean). Bottom row: within-patient heterogeneity (MAD of image-level deviations from patient mean). Left column: CLR tumors. Right column: DII tumors.

Beyond estimating spatial interactions, SHADE's conditional intensity functions enable prediction of target cell spatial distributions from source cell configurations. Predictive performance varied by cell type and tumor subtype, with all target cell types showing higher prediction accuracy in CLR versus DII tumors (Supplement Section 5.3).

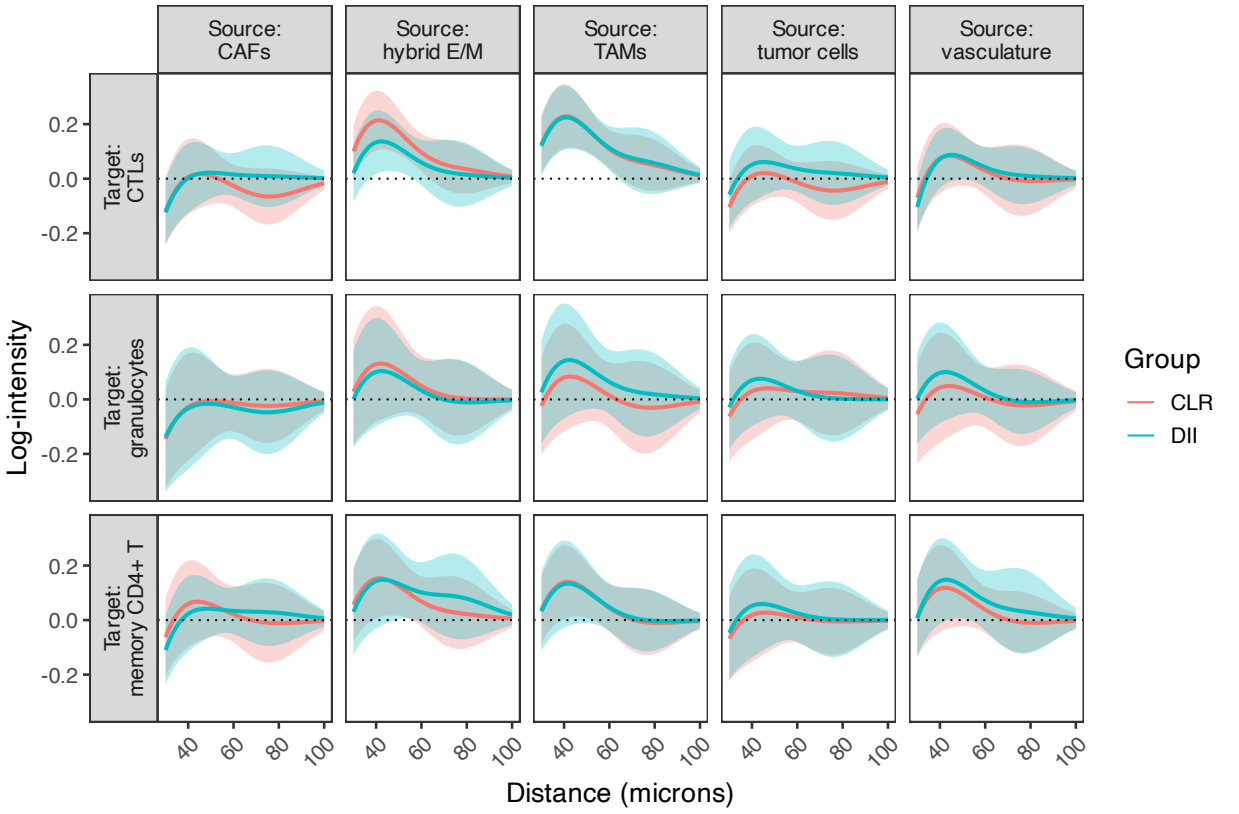

Figure 9: Cohort-level SICs ($\psi_{t_1 \to t_2}^{(g,p)}$) estimated for all source–target cell type pairs in the CRC dataset, stratified by CLR and DII patient groups, with simultaneous 95% credible bands.

4.5 Comparing SHADE to traditional G-cross-based spatial clustering analysis

To contextualize our SHADE results, we performed an alternative analysis using the G-cross function [Baddeley et al., 2015], a nonparametric estimator of cross-type clustering commonly used in spatial point pattern analysis. This comparison highlights how SHADE differs from traditional methods in its modeling framework and interpretability of results.

For each tissue section, we computed G-cross estimates at distances from 0 to 80 microns and extracted values at key distances (20, 40, 60 microns) for comparison. To quantify whether differences in clustering could predict patient group (CLR vs DII), we fitted logistic regression models with G-cross as the predictor and used FDR-adjusted p-values to identify

significant associations. The resulting estimates are visualized as a heatmap of log-odds ratios (log-ORs), indicating the strength and direction of group differences in clustering at each distance.

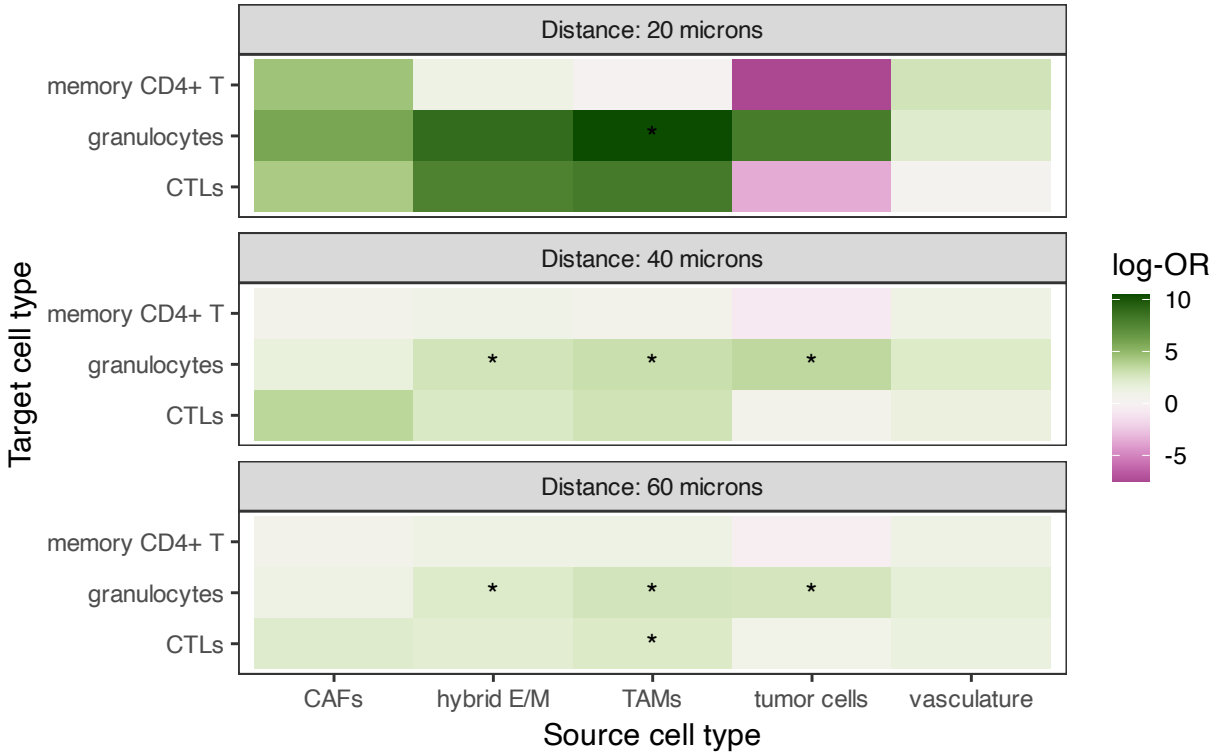

Figure 10: Heatmap of log-odds ratios (log-ORs) from logistic regression models comparing G-cross clustering metrics between CLR and DII patient groups, stratified by distance (20, 40, 60 microns). Tiles represent the estimated log-OR for each source–target pair at a given distance, with asterisks indicating significant differences ($p < 0.05$, FDR-adjusted). Green indicates stronger clustering in DII, purple indicates stronger clustering in CLR.

The G-cross-based analysis (Figure 10) reveals several patterns of cell–cell clustering between CLR and DII patients. For instance, TAM–granulocyte interactions showed strong, statistically significant differences at all examined distances (20–60 microns), with higher clustering in DII tumors. SHADE's directional analysis shows concordant results, with DII patients exhibiting greater attraction of granulocytes to TAMs across all distances, suggesting that this marginal clustering pattern reflects genuine directional spatial association. However, G-cross and SHADE diverge for other interactions. SHADE identified stronger CTL-tumor clustering in DII patients and differential stromal interactions (e.g., CTL re-

pulsion from CAFs being stronger in CLR at medium-long range), patterns that are less evident or show different magnitudes in the G-cross analysis. These discrepancies may reflect SHADE's multivariate adjustment for confounding cell types and hierarchical modeling structure, which can reveal conditional dependencies that differ from marginal pairwise associations captured by G-cross.

5 Discussion

In this work, we introduced SHADE, a Bayesian hierarchical model for quantifying asymmetric spatial interactions in multiplexed imaging data. By modeling the conditional intensity function and estimating spatial interaction curves, our approach enables the identification of directional associations between cell types while accounting for multilevel variation across images, patients, and cohorts.

Through simulation studies, we demonstrated that SHADE effectively captures asymmetric spatial associations while leveraging hierarchical structure to improve estimation. Including multilevel priors improves inference accuracy by reducing bias and variance in estimated coefficients. SHADE also demonstrated superior robustness to low cell densities and limited sampling, consistently outperforming G-cross, L-cross and flat models in detecting true spatial interactions across diverse simulation conditions.

A key advantage of SHADE over traditional spatial summary statistics is its ability to formally model and quantify heterogeneity across biological scales. While methods such as Ripley's K-function and the G-cross function can compute separate estimates for each image and then compare them post-hoc, SHADE's hierarchical Bayesian framework enables joint estimation with partial pooling, explicit variance decomposition, and formal quantification of between-patient and within-patient variability (Section 4.3). This distinction is crucial for biomedical datasets where spatial patterns exhibit systematic variation across patients and tissue sections, and where borrowing strength across the hierarchy improves estimation

efficiency and enables more nuanced biological inference. .

SHADE revealed distinct patterns of cellular organization differentiating immune-infiltrated (CLR) and immune-excluded (DII) colorectal tumors. DII tumors showed elevated CTL-tumor spatial association across all distances, potentially reflecting failed immune surveillance or exhausted T cell retention, along with greater granulocyte-TAM clustering suggesting enhanced immunosuppressive myeloid networks. In contrast, CLR tumors demonstrated stronger CTL attraction to hybrid E/M cells at short ranges and greater immune-stromal spatial segregation, with CTLs and memory CD4+ T cells showing stronger repulsion from CAFs and hybrid E/M cells at medium-to-long ranges. Given CAFs' role in immune suppression and barrier formation, these patterns may indicate more effective compartmentalization of immune and suppressive elements in CLR tumors, whereas reduced segregation in DII could reflect barrier disruption or exclusionary mechanisms constraining immune access.

Beyond cohort-level differences, we also found substantial heterogeneity in spatial organization across patients and across tissue sections from the same patient. This variability was particularly pronounced in granulocyte interactions with TAMs, vasculature, and hybrid E/M cells, suggesting patient-specific or localized microenvironmental factors influencing spatial localization. Finally, SHADE's ability to predict target cell distributions from spatial covariates varied by cell type and tumor subtype: immune cell organization was more predictable in CLR tumors, indicating more structured immune environments compared to the more disorganized spatial context of DII tumors. These findings illustrate both consistent interaction motifs and biologically meaningful variability across spatial scales in tumor immune landscapes.

Comparisons with G-cross function estimates and multilevel functional PCA (Section 5.5.3) illustrate SHADE's complementary value. Both SHADE and marginal summary statistics identified granulocyte-TAM clustering in DII tumors, but diverged for other interactions where SHADE's multivariate adjustment revealed conditional dependencies obscured in marginal analyses (e.g., CTL-tumor clustering, CTL-CAF repulsion in CLR). While SHADE

provides a generative probabilistic model with conditional intensity estimation and partial pooling for improved precision, functional data methods offer model-free characterization of variation in marginal pairwise statistics. These approaches are complementary rather than competing: the choice depends on whether the goal is mechanistic understanding of conditional dependencies or descriptive analysis of marginal spatial patterns.

A key strength of SHADE is its flexibility in modeling directional interactions across spatial scales, avoiding the restrictive symmetry assumptions of traditional spatial models. Moreover, the use of logistic regression for conditional intensity estimation allows for scalable and stable inference, sidestepping common numerical pitfalls of direct Poisson modeling.

Nonetheless, SHADE has limitations. First, while SICs capture directional spatial association, they remain correlational and cannot determine causality or infer mechanisms of interaction. Second, the SICs reflect spatial dependence rather than molecular signaling pathways, which may limit biological interpretability in some settings. Third, although SHADE supports biologically motivated conditioning structures, exploratory analyses may benefit from modeling both directions of association when directionality is uncertain. Fourth, hierarchical shrinkage produces credible intervals that are narrower than marginal image-level intervals, reflecting the precision-accuracy tradeoff inherent in borrowing strength across images (see Supplement Section 4.9).

Future extensions of SHADE could incorporate functional covariates—such as marker intensity, proliferation, or exhaustion scores—into the SIC framework, enabling joint analysis of spatial structure and functional state. This would open the door to modeling not just where cells are, but how they behave spatially in context. Additionally, where cell segmentation boundaries are available, boundary-to-boundary distances could be used in place of centroid-to-centroid distances, further reducing geometric crowding effects at short spatial ranges and improving biological interpretability of near-contact interactions.

Overall, our results highlight the importance of capturing asymmetric and hierarchical structure in spatial models, and position SHADE as a powerful tool for dissecting the complex

architecture of tissue microenvironments in cancer and beyond.

Acknowledgements

Competing Interests

I have read the journal's policy and the authors of this manuscript have the following competing interests: A. Rao serves as a member for Voxel Analytics LLC and consults for Telperian, Tempus Inc. and TCS Ltd.

Funding

J. Eliason was funded by NIH-NCI 5 R01-CA268426–03, R37CA214955-01A1, NSF Award Number 215776 and Advanced Proteogenomics of Cancer (T32 CA140044). A. Rao was supported by CCSG Bioinformatics Shared Resource 5 P30 CA046592, a gift from Agilent technologies, and a Precision health Investigator award from U-M Precision Health, NCI Grant R37-CA214955, The University of Michigan (UM) startup institutional research funds and Research Scholar Grant from the American Cancer Society (RSG-16-005-01).

References

A. Baddeley and R. Turner. spatstat: An R Package for Analyzing Spatial Point Patterns. *Journal of Statistical Software*, 12:1–42, Jan. 2005. ISSN 1548-7660. doi: 10.18637/jss.v012.i06. URL `https://doi.org/10.18637/jss.v012.i06`.

A. Baddeley, J.-F. Coeurjolly, E. Rubak, and R. Waagepetersen. Logistic regression for spatial Gibbs point processes. *Biometrika*, 101(2):377–392, June 2014. ISSN 0006-3444. doi: 10.1093/biomet/ast060. URL `https://doi.org/10.1093/biomet/ast060`.

A. Baddeley, E. Rubak, and R. Turner. *Spatial Point Patterns: Methodology and Applications with R*. CRC Press, Nov. 2015. ISBN 978-1-4822-1021-7. Google-Books-ID: rGbmCgAAQBAJ.

R. Bagchi and J. B. Illian. A method for analysing replicated point patterns in ecology. *Methods in Ecology and Evolution*, 6(4):482–490, 2015. ISSN 2041-210X. doi: 10.1111/2041-210X.12335.

S. Barua, P. Fang, A. Sharma, J. Fujimoto, I. Wistuba, A. U. K. Rao, and S. H. Lin. Spatial Interaction of Tumor Cells and Regulatory T cells Correlates with Survival in Non-Small Cell Lung Cancer. *Lung cancer (Amsterdam, Netherlands)*, 117:73–79, Mar. 2018. ISSN 0169-5002. doi: 10.1016/j.lungcan.2018.01.022.

M. L. Bell and G. K. Grunwald. Mixed models for the analysis of replicated spatial point patterns. *Biostatistics*, 5(4):633–648, Oct. 2004. ISSN 1465-4644. doi: 10.1093/biostatistics/kxh014.

G. Bindea, B. Mlecnik, M. Tosolini, A. Kirilovsky, M. Waldner, A. C. Obenauf, H. Angell, T. Fredriksen, L. Lafontaine, A. Berger, P. Bruneval, W. H. Fridman, C. Becker, F. Pagès, M. R. Speicher, Z. Trajanoski, and J. Galon. Spatiotemporal Dynamics of Intratumoral Immune Cells Reveal the Immune Landscape in Human Cancer. *Immunity*, 39(4):782–795, Oct. 2013. ISSN 1074-7613. doi: 10.1016/j.immuni.2013.10.003. URL `https://www.cell.com/immunity/abstract/S1074-7613(13)00437-8`. Publisher: Elsevier.

M. Binnewies, E. W. Roberts, K. Kersten, V. Chan, D. F. Fearon, M. Merad, L. M. Coussens, D. I. Gabrilovich, S. Ostrand-Rosenberg, C. C. Hedrick, R. H. Vonderheide, M. J. Pittet, R. K. Jain, W. Zou, T. K. Howcroft, E. C. Woodhouse, R. A. Weinberg, and M. F. Krummel. Understanding the tumor immune microenvironment (TIME) for effective therapy. *Nature Medicine*, 24(5):541–550, May 2018. ISSN 1546-

170X. doi: 10.1038/s41591-018-0014-x. URL https://www.nature.com/articles/s41591-018-0014-x. Publisher: Nature Publishing Group.

N. P. Canete, S. S. Iyengar, J. T. Ormerod, H. Baharlou, A. N. Harman, and E. Patrick. spicyR: Spatial analysis of *in situ* cytometry data in R. *Bioinformatics*, 38(11):3099–3105, May 2022. ISSN 1367-4803, 1367-4811. doi: 10.1093/bioinformatics/btac268.

Z. Cao, S. Quazi, S. Arora, L. D. Osellame, I. J. Burvenich, P. W. Janes, and A. M. Scott. Cancer-associated fibroblasts as therapeutic targets for cancer: advances, challenges, and future prospects. *Journal of Biomedical Science*, 32(1):7, Jan. 2025. ISSN 1423-0127. doi: 10.1186/s12929-024-01099-2. URL https://doi.org/10.1186/s12929-024-01099-2.

J. Gabry, R. Češnovar, A. Johnson, and S. Bronder. *cmdstanr: R Interface to 'CmdStan'*, 2024. URL https://mc-stan.org/cmdstanr/. R package version 0.8.1, https://discourse.mc-stan.org.

P. Grabarnik and A. Särkkä. Modelling the spatial structure of forest stands by multivariate point processes with hierarchical interactions. *Ecological Modelling*, 220(9):1232–1240, May 2009. ISSN 0304-3800. doi: 10.1016/j.ecolmodel.2009.02.021. URL https://www.sciencedirect.com/science/article/pii/S0304380009001537.

H. Högmander and A. Särkkä. Multitype Spatial Point Patterns with Hierarchical Interactions. *Biometrics*, 55(4):1051–1058, 1999. ISSN 1541-0420. doi: 10.1111/j.0006-341X.1999.01051.x. URL https://onlinelibrary.wiley.com/doi/abs/10.1111/j.0006-341X.1999.01051.x. _eprint: https://onlinelibrary.wiley.com/doi/pdf/10.1111/j.0006-341X.1999.01051.x.

J. B. Illian and D. K. Hendrichsen. Gibbs point process models with mixed effects. *Environmetrics*, 21(3-4):341–353, 2010. ISSN 1099-095X. doi: 10.1002/env.1008.

A. L. Janeiro, E. M. Wong, D. Jiménez-Sánchez, C. O. de Solorzano, M. D. Lozano, A. Teijeira, K. A. Schalper, I. Melero, and C. E. D. Andrea. Spatially resolved tissue imaging to

analyze the tumor immune microenvironment: Beyond cell-type densities. *Journal for ImmunoTherapy of Cancer*, 12(5), May 2024. ISSN 2051-1426. doi: 10.1136/jitc-2023-008589.

S.-y. Jing, H.-q. Wang, P. Lin, J. Yuan, Z.-x. Tang, and H. Li. Quantifying and interpreting biologically meaningful spatial signatures within tumor microenvironments. *npj Precision Oncology*, 9(1):68, Mar. 2025. ISSN 2397-768X. doi: 10.1038/s41698-025-00857-1.

N. A. Kuburich, J. M. Kiselka, P. den Hollander, A. A. Karam, and S. A. Mani. The Cancer Chimera: Impact of Vimentin and Cytokeratin Co-Expression in Hybrid Epithelial/Mesenchymal Cancer Cells on Tumor Plasticity and Metastasis. *Cancers*, 16 (24):4158, Dec. 2024. ISSN 2072-6694. doi: 10.3390/cancers16244158. URL `https://www.ncbi.nlm.nih.gov/pmc/articles/PMC11674825/`.

A. Lee, A. Särkkä, T. M. Madhyastha, and T. J. Grabowski. Characterizing cross-subject spatial interaction patterns in functional magnetic resonance imaging studies: A two-stage point-process model. *Biometrical journal. Biometrische Zeitschrift*, 59(6):1352–1381, Nov. 2017. ISSN 0323-3847. doi: 10.1002/bimj.201600212.

C. C. Maley, A. Aktipis, T. A. Graham, A. Sottoriva, A. M. Boddy, M. Janiszewska, A. S. Silva, M. Gerlinger, Y. Yuan, K. J. Pienta, K. S. Anderson, R. Gatenby, C. Swanton, D. Posada, C.-I. Wu, J. D. Schiffman, E. S. Hwang, K. Polyak, A. R. A. Anderson, J. S. Brown, M. Greaves, and D. Shibata. Classifying the evolutionary and ecological features of neoplasms. *Nature Reviews Cancer*, 17(10):605–619, Oct. 2017. ISSN 1474-1768. doi: 10.1038/nrc.2017.69. URL `https://www.nature.com/articles/nrc.2017.69`. Publisher: Nature Publishing Group.

J. Moller and R. P. Waagepetersen. *Statistical Inference and Simulation for Spatial Point Processes*. Chapman and Hall/CRC, New York, Sept. 2003. ISBN 978-0-203-49693-0. doi: 10.1201/9780203496930.

M. Myllymäki, A. Särkkä, and A. Vehtari. Hierarchical second-order analysis of replicated

spatial point patterns with non-spatial covariates. *Spatial Statistics*, 8:104–121, May 2014. ISSN 2211-6753. doi: 10.1016/j.spasta.2013.07.006.

S. Samorodnitsky, K. Campbell, A. Ribas, and M. C. Wu. A Spatial Omnibus Test (SPOT) for Spatial Proteomic Data. *Bioinformatics*, 40(7):btae425, July 2024. ISSN 1367-4811. doi: 10.1093/bioinformatics/btae425.

C. M. Schürch, S. S. Bhate, G. L. Barlow, D. J. Phillips, L. Noti, I. Zlobec, P. Chu, S. Black, J. Demeter, D. R. McIlwain, S. Kinoshita, N. Samusik, Y. Goltsev, and G. P. Nolan. Coordinated Cellular Neighborhoods Orchestrate Antitumoral Immunity at the Colorectal Cancer Invasive Front. *Cell*, 182(5):1341–1359.e19, Sept. 2020. ISSN 1097-4172. doi: 10.1016/j.cell.2020.07.005.

S. Seal, B. Neelon, P. M. Angel, E. C. O'Quinn, E. Hill, T. Vu, D. Ghosh, A. S. Mehta, K. Wallace, and A. V. Alekseyenko. SpaceANOVA: Spatial Co-occurrence Analysis of Cell Types in Multiplex Imaging Data Using Point Process and Functional ANOVA. *Journal of Proteome Research*, 23(4):1131–1143, Apr. 2024. ISSN 1535-3893. doi: 10.1021/acs.jproteome.3c00462.

W. Sheng, C. Zhang, T. M. Mohiuddin, M. Al-Rawe, F. Zeppernick, F. H. Falcone, I. Meinhold-Heerlein, and A. F. Hussain. Multiplex Immunofluorescence: A Powerful Tool in Cancer Immunotherapy. *International Journal of Molecular Sciences*, 24(4):3086, Feb. 2023. ISSN 1422-0067. doi: 10.3390/ijms24043086. URL `https://www.ncbi.nlm.nih.gov/pmc/articles/PMC9959383/`.

A. C. Soupir, I. V. Gadiyar, B. R. Helm, C. R. Harris, S. N. Vandekar, L. C. Peres, R. J. Coffey, J. Wrobel, S. Ma, and B. L. Fridley. Benchmarking Spatial Co-Localization Methods for Single-Cell Multiplex Imaging Data with Applications to High-Grade Serous Ovarian and Triple Negative Breast Cancer. *Statistics and Data Science in Imaging*, 2(1):2437947, 2025. ISSN 2997-9676. doi: 10.1080/29979676.2024.2437947.

Stan Development Team. *Stan Reference Manual*, 2024. URL https://mc-stan.org. version 2.36.0.

A. P. Tsang, S. N. Krishnan, J. N. Eliason, J. J. McGue, A. Qin, T. L. Frankel, and A. Rao. Assessing the Tumor Immune Landscape Across Multiple Spatial Scales to Differentiate Immunotherapy Response in Metastatic Non-Small Cell Lung Cancer. *Laboratory Investigation*, 104(11):102148, Nov. 2024. ISSN 0023-6837. doi: 10.1016/j.labinv.2024.102148. URL https://www.sciencedirect.com/science/article/pii/S0023683724018269.

T. Vu, J. Wrobel, B. G. Bitler, E. L. Schenk, K. R. Jordan, and D. Ghosh. SPF: A spatial and functional data analytic approach to cell imaging data. *PLOS Computational Biology*, 18(6):e1009486, June 2022. ISSN 1553-7358. doi: 10.1371/journal.pcbi.1009486.

J. Wrobel, A. C. Soupir, M. T. Hayes, L. C. Peres, T. Vu, A. Leroux, and B. L. Fridley. Mxfda: A comprehensive toolkit for functional data analysis of single-cell spatial data. *Bioinformatics Advances*, 4(1):vbae155, Jan. 2024. ISSN 2635-0041. doi: 10.1093/bioadv/vbae155.

Y. Yuan. Spatial Heterogeneity in the Tumor Microenvironment. *Cold Spring Harbor Perspectives in Medicine*, 6(8):a026583, Aug. 2016. ISSN 2157-1422. doi: 10.1101/cshperspect.a026583. URL https://www.ncbi.nlm.nih.gov/pmc/articles/PMC4968167/.

Supporting Information

S1 File. Supplementary Materials. Contains supplementary methods (background on Gibbs point process models, logistic regression approximation, simultaneous credible band construction, extended simulation methods), supplementary results (hyperparameter studies, coverage and Type I error analysis, robustness to spatial confounding), extended colorectal cancer analysis results, and comparison with multilevel functional PCA methodology.